

Article

# Application of the Hyperspectral Imager for the Coastal Ocean to Phytoplankton Ecology Studies in Monterey Bay, CA, USA

John P. Ryan <sup>1,\*</sup>, Curtiss O. Davis <sup>2</sup>, Nicholas B. Tufillaro <sup>2</sup>, Raphael M. Kudela <sup>3</sup>  
and Bo-Cai Gao <sup>4</sup>

<sup>1</sup> Monterey Bay Aquarium Research Institute, 7700 Sandholdt Road, Moss Landing, CA 95039, USA

<sup>2</sup> College of Earth, Ocean and Atmospheric Sciences, Oregon State University, 104 CEOAS Admin. Bldg., Corvallis, OR 97331, USA; E-Mails: cdavis@coas.oregonstate.edu (C.O.D); nbt@coas.oregonstate.edu (N.B.T)

<sup>3</sup> Ocean Science Department, University of California, Santa Cruz, 1156 High Street, Santa Cruz, CA 95064, USA; E-Mail: kudela@ucsc.edu

<sup>4</sup> Remote Sensing Division, Code 7232, Naval Research Laboratory, Washington, DC 20375, USA; E-Mail: gao@nrl.navy.mil

\* Author to whom correspondence should be addressed; E-Mail: ryjo@mbari.org;  
Tel.: +1-831-775-1978; Fax: +1-831-775-1620.

Received: 8 November 2013; in revised form: 24 December 2013 / Accepted: 23 January 2014 /  
Published: 27 January 2014

---

**Abstract:** As a demonstrator for technologies for the next generation of ocean color sensors, the Hyperspectral Imager for the Coastal Ocean (HICO) provides enhanced spatial and spectral resolution that is required to understand optically complex aquatic environments. In this study we apply HICO, along with satellite remote sensing and *in situ* observations, to studies of phytoplankton ecology in a dynamic coastal upwelling environment—Monterey Bay, CA, USA. From a spring 2011 study, we examine HICO-detected spatial patterns in phytoplankton optical properties along an environmental gradient defined by upwelling flow patterns and along a temporal gradient of upwelling intensification. From a fall 2011 study, we use HICO’s enhanced spatial and spectral resolution to distinguish a small-scale “red tide” bloom, and we examine bloom expansion and its supporting processes using other remote sensing and *in situ* data. From a spectacular HICO image of the Monterey Bay region acquired during fall of 2012, we present a suite of algorithm results for characterization of phytoplankton, and we examine the strengths, limitations, and distinctions of each algorithm in the context of the enhanced spatial and spectral resolution.

**Keywords:** phytoplankton; remote sensing; Monterey Bay; upwelling

---

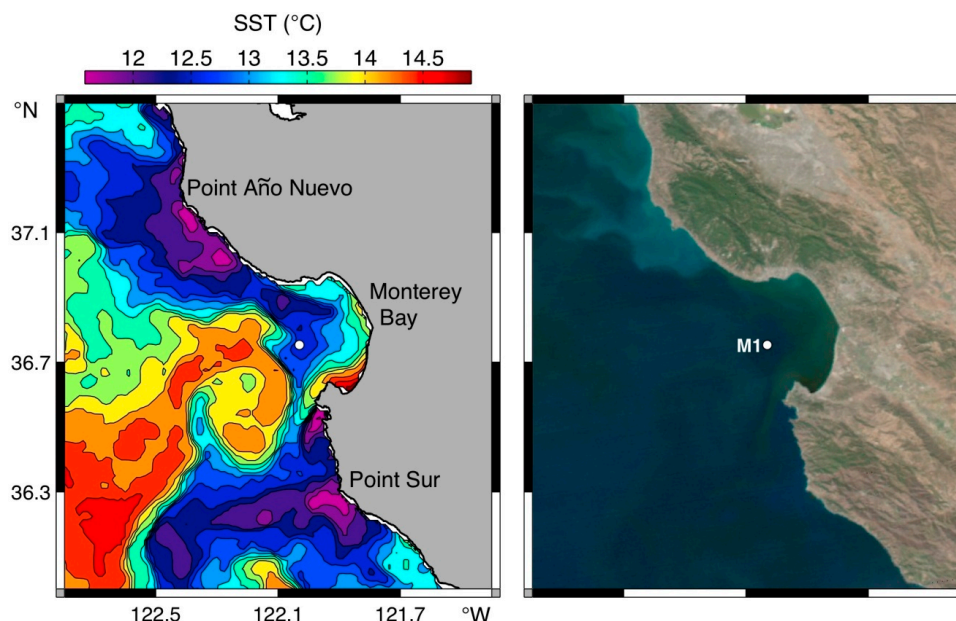
## 1. Introduction

The Hyperspectral Imager for the Coastal Ocean (HICO) is the first spaceborne imaging spectrometer designed for coastal ocean research [1,2]. Sponsored by the Office of Naval Research as an Innovative Naval Prototype, HICO was developed to demonstrate improved coastal remote sensing products including bathymetry, bottom types, water optical properties, and on-shore vegetation maps. Enhanced products are supported by HICO's spatial resolution ( $<100 \times 100$  m), spectral resolution (400 to 900 nm sampled at 5.7 nm) and signal-to-noise ratio ( $>200:1$  for a 5% albedo scene). Based on the Portable Hyperspectral Imager for Low-Light Spectroscopy (PHILLS) airborne imaging spectrometers [3], HICO demonstrates innovative ways to reduce the cost and schedule of a space mission, by adapting proven aircraft imager architecture and using commercial off-the-shelf components. HICO was installed on the International Space Station (ISS) on 23 September 2009 and collected its first images the following day. HICO observations have since been targeted for a wide variety of environments. Here we focus on the application of HICO capabilities to the measurement of water optical properties and characterization of phytoplankton in a highly productive coastal system.

The study region, Monterey Bay, California (Figure 1) is the largest open embayment along the west coast of the USA. It is located in the central California Current System (CCS). Wind driven upwelling of nutrient-rich deep water in coastal upwelling systems like the CCS supports high levels of primary productivity [4]. Most of the wind-driven upwelling supply to Monterey Bay originates from upwelling centers north and south of the bay [5,6]. These upwelling centers are shown in Figure 1 as the regions where cold upwelling plumes emanate from the coast: Point Año Nuevo and Point Sur. Additionally, upwelling within the bay occurs in response to strong diurnal forcing by the sea breeze [7], and in response to internal oscillations over Monterey Canyon that transport deep water onto the shelf [8,9]. In addition to supporting great fisheries, coastal upwelling systems host a variety of harmful algal bloom (HAB) types [10]. In Monterey Bay, blooming of toxigenic diatoms has been directly linked to wind-driven upwelling [11], and blooming of a dinoflagellate species that can cause massive mortality of seabirds [12] has been linked to canyon upwelling [9]. Additionally, anthropogenic nutrient sources regulate toxicity of HAB diatoms [13] as well as bloom dynamics of a dinoflagellate species linked to seabird mortality [14].

The diversity and variability of natural and anthropogenic forcing in the Monterey Bay region creates tremendous ecological complexity. This complexity motivates advancement of methods. In this study, we show how the enhanced spatial and spectral resolution of HICO supports methods to advance understanding of this complex environment. Using studies during the contrasting seasons of spring and fall, we illustrate processes of phytoplankton ecology by integrating algorithm results derived from HICO data with multidisciplinary satellite remote sensing and *in situ* observations.

**Figure 1.** Overview of the study region. Thermal (AVHRR) and color (MODIS Aqua) images were acquired on 13 October 2008, at 11:04 and 14:20 local time, respectively, during a bloom of toxigenic diatoms [11].



## 2. Materials and Methods

### 2.1. HICO Image Acquisition and Processing

HICO is a demonstration sensor, and data are collected for particular study areas from a target list compiled by Naval Research Laboratory (NRL) personnel with input from Navy, academic, and international partners. The standard HICO scene is  $42 \times 192$  km, and a maximum of one scene is collected on each 90-min orbit. Data requests are compiled by NRL and sent by NASA to the ISS for execution. Data is transmitted from the ISS to NASA Marshall Space Flight Center and then to NRL in Washington DC for processing. The initial processing from level 0 (raw data) to level 1b (calibrated radiances with geolocation information) includes dark current subtraction, CCD smear correction, second-order correction, spectral calibration, and radiance calibration. We requested data collections for Monterey Bay and obtained the HICO data from Oregon State University [15].

For atmospheric correction (AC) of HICO images we used two software implementations, the ATmosphere REMoval (ATREM) algorithm [16], and Tafkaa 6s [17]. The purpose of applying multiple AC implementations was to evaluate (1) the quality and sensitivity of AC results relative to *in situ* optical measurements, and (2) results from phytoplankton characterization algorithms that employ different regions of the spectrum (Section 2.2). Limitations in HICO radiometric calibration required modification of the application of ATREM. A continental aerosol correction with a visibility of 300 km (resulting in an aerosol optical depth at 550 nm of 0.0853) was applied based on solar and viewing geometry to obtain an intermediate reflectance spectrum. The mean value of intermediate reflectance for eight narrow channels near 760 nm was calculated. This mean value was subtracted from the intermediate reflectance spectrum for all channels to retrieve water-leaving reflectance. This method effectively removed effects of sun glint, thin clouds and fog, and the spectrally independent portion of

aerosol effects (such as those from large oceanic particles). In addition to this modified computation, ATREM also computed and corrected for atmospheric gas absorption. For a direct comparison to the ATREM results, Tafkaa 6s was similarly configured. For comparison with *in situ* spectra acquired during the fall 2011 study, we also examined spectra from a 26 October HICO image processed using standard NASA ocean color algorithms for the MODIS channels derived from the HICO spectra. This image was acquired from the NASA ocean color website.

Atmospherically corrected HICO images of Monterey Bay contained a cross-track offset that depended on wavelength as well as solar and viewing geometry. For bands above 550 nm, this offset was small, less than 1% of normalized water leaving radiance (nLw), but between 550 and 400 nm the offset increased monotonically. The additional signal in the blue is thought to be a polarization dependent artifact specific to the HICO sensor [18]. We corrected for the cross-track artifact using an empirical procedure that computes a wavelength dependent quadratic function from cloud-free cross-track scans and applies the correction to all cross-track scans. For geolocation of HICO image pixels, we used the geometry data provided with each image as well as ground control points. This procedure located pixels to within 2–3 pixels (a few hundred meters).

## 2.2. Algorithms for Phytoplankton Characterization

We employed a suite of algorithms for characterization of phytoplankton from remote sensing of ocean color, using single 5.7 nm HICO bands whose center wavelengths were closest to those used with multispectral data (Table 1). The longest standing characterization is the band-ratio chlorophyll algorithm that uses the blue-green region of the spectrum. Specifically, we used the OC4 chlorophyll algorithm [19]. To quantify inherent optical properties (IOPs), we used a quasi-analytical algorithm [20,21], specifically Version 5 [22]. IOP computations used a reference wavelength of 555 nm. The chlorophyll and IOP calculations used remote sensing reflectance resulting from ATREM, followed by cross-track illumination correction (Section 2.1). Additionally we examined results from a suite of linear baseline algorithms that employ the red to near-infrared region of the spectrum. These were chlorophyll fluorescence line height (FLH) computed using bands corresponding to both the MODIS and MERIS multispectral sensors and the maximum chlorophyll index (MCI) used to detect intense “red tide” blooms by their reflectance peak in the near-infrared [23,24]. For all linear baseline results, we used nLw resulting from Tafkaa, followed by cross-track illumination correction (Section 2.1).

**Table 1.** Center wavelengths of Hyperspectral Imager for the Coastal Ocean (HICO) bands used in algorithm computations.

	Chlorophyll	QAA IOP	MODIS FLH	MERIS FLH	MERIS MCI
Multispectral bands (nm)	443, 490, 510, 555	411, 443, 490, 555, 667	665, 677, 746	665, 681, 709	681, 709, 754
HICO bands (nm)	444, 490, 507, 553	410, 444, 490, 553, 668	668, 679, 748	668, 679, 708	679, 708, 753

## 2.3. Satellite Observations

To extend characterization of the ecology of a nascent “extreme bloom” detected by HICO, we used MERIS MCI (Section 2.2). These images were computed from MERIS Level 2 radiance data using the ESA BEAM software. To examine regional sea surface temperature (SST) patterns, we used data from



the Advanced Very High Resolution Radiometer (AVHRR) constellation of sensors. The AVHRR processing methods applied in this study are documented elsewhere [25].

#### 2.4. *In Situ Observations*

Observations from the M1 mooring at the mouth of Monterey Bay (Figure 1) were used for study context, as well as direct comparison with HICO results. Specifically, we used measurements of surface wind speed and direction, water column temperature and salinity, and near-surface (1 m) chlorophyll fluorescence. Details of M1 sensors are documented elsewhere [11]. Hourly data were daily-averaged. During the spring 2011 study, we used high-resolution multidisciplinary water column observations acquired by the *Dorado* autonomous underwater vehicle (AUV). Details of *Dorado* and its sensing suite are available in earlier publications [9,26]. During our fall 2011 study, *in situ* hyperspectral optical ground truth measurements were made using a Satlantic HyperPro II profiling radiometer. Vertical profiles were binned to 10 cm resolution and propagated to the surface using the ProSoft software standard processing. Remote sensing reflectance was determined using the surface reference sensor and the propagated nLw values from the profile.

### 3. Results and Discussion

#### 3.1. *Environmental Overview for 2011*

Wind forcing and oceanic response during 2011 at mooring M1 (Figure 1) provide context for the spring and fall studies (Figure 2). Upwelling favorable (alongshore, equatorward) winds were most persistently directed and strongest during April–May. The oceanic response to this wind forcing is evident as the minimum temperatures and maximum salinities in the upper water column, also during April and May (Figure 2). These relatively cold and saline conditions reflect the presence of deep water upwelled to the surface (Figure 1). Our spring study took place during this period of maximum upwelling. Progressing through the summer and into the fall, average wind speed decreased, wind direction became more variable, and the warmest surface conditions of the year developed during October (Figure 2). Our fall study took place during this warm period.

#### 3.2. *Spring 2011 Study*

During the spring study, three HICO images were acquired within an eight-day period (times shown in Figure 2). During this period, 25 April to 3 May, wind forcing transitioned from a brief relaxation/reversal to the strongest upwelling-favorable winds of the year (Figure 2). The regional response to upwelling intensification was likewise strong, as evidenced in water column temperature and salinity at M1 (Figure 2) and regional SST (Figure 3). Flow from the upwelling centers north and south of the bay generated strong cooling throughout the region, and much upwelled water entered the bay, primarily from the Point Año Nuevo upwelling center to the north (Figure 3).

Mooring M1 was in the path of this upwelling flow (Figure 3), and its sensors detected not only the cooling, but also a decline in chlorophyll fluorescence (Figure 4). Variation in chlorophyll fluorescence at M1 occurred at two dominant time scales. One time scale was that of the transition to from relatively warm, high-chlorophyll conditions during 24–28 April to relatively cool, low-chlorophyll conditions

after 28 April. This was associated with influx of recently upwelled water (Figure 3), which is typically low in phytoplankton abundance. The second time scale was approximately diurnal (Figure 4). While diurnal variation in chlorophyll fluorescence may have a physiological basis, this bio-optical variation coincided with similar diurnal variation in temperature during much of the record. This suggests that variation at this time scale was associated primarily with a physical process having a quasi-diurnal frequency, such as advection of gradients. This is supported by the synoptic patterns of chlorophyll fluorescence line height (FLH) in the HICO images, particularly those for 25 and 27 April (Figure 4b,c). M1 was amid strong horizontal gradients in FLH, thus periodic currents caused by tidal and/or diurnal wind forcing would have cyclically advected local gradients and caused the oscillatory signal at M1.

**Figure 2.** Environmental context for HICO results, from mooring M1 (Figure 1). Wind speed and direction are represented by the length and orientation of the vectors, respectively (vectors point in the direction the wind). Times of all HICO images acquired during 2011 are shown along the top time axis as open diamonds, and times of those images examined in this study are shown as filled diamonds.

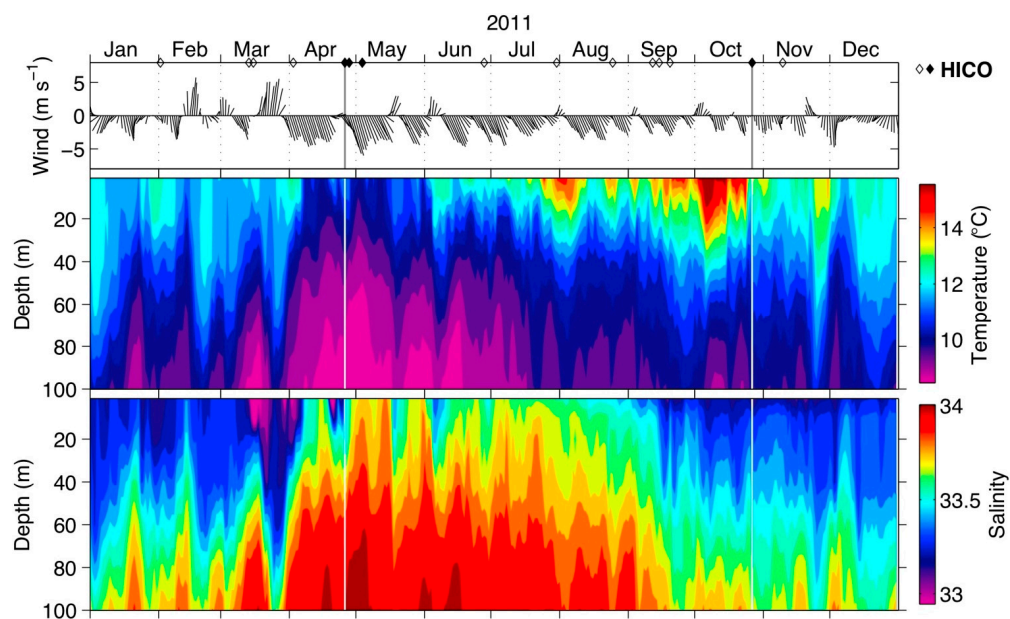


**Figure 3.** Upwelling intensification during the spring 2011 study. Sea surface temperature (SST) images are from AVHRR; times are local.

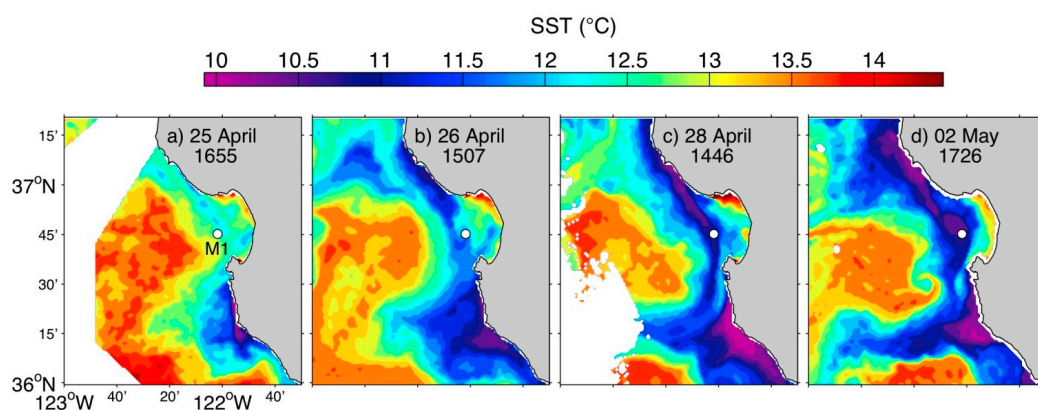
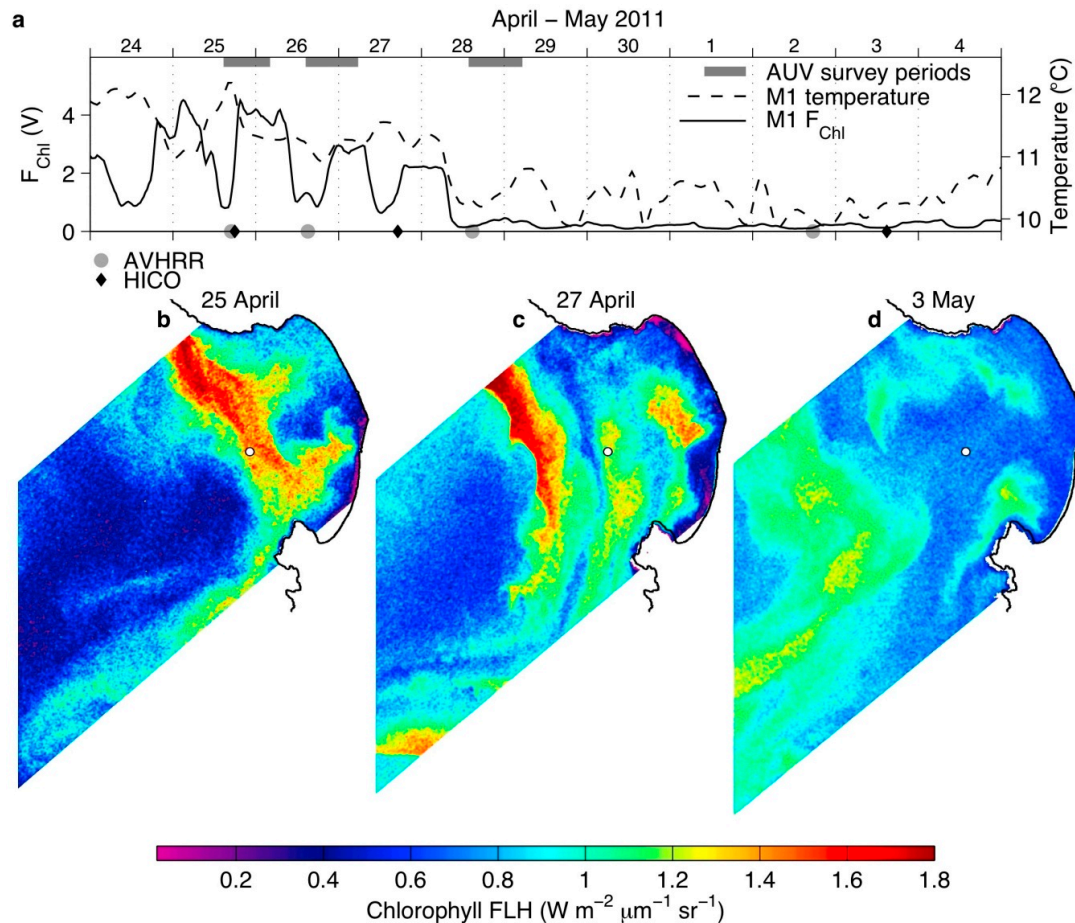


**Figure 4.** Spring 2011 study: Changes in local and regional conditions associated with upwelling intensification (Figure 3). **(a)** Measurements from 1 m depth at mooring M1;  $F_{Chl}$  is raw signal from the chlorophyll fluorometer. **(b–d)** FLH computed using HICO bands nearest those of MODIS FLH (Table 1); the white circle indicates M1 location.

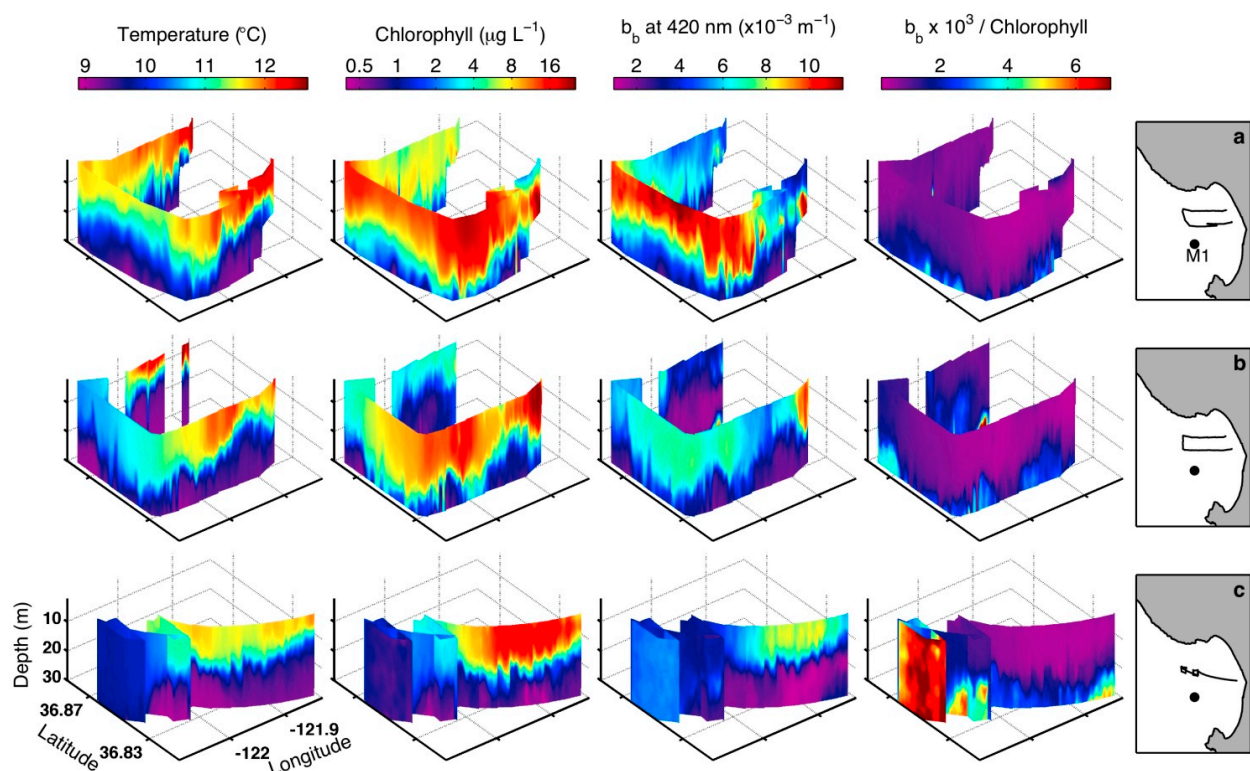


While the fixed-point time series at M1 suggests a simple response of decreasing chlorophyll fluorescence in association with the upwelling event, the HICO spring time-series reveals great patchiness developing throughout the region (Figure 4). Regions of relatively high FLH moved both offshore and into the central bay between 25 and 27 April (Figure 4b,c), consistent with the bifurcated flow that typically develops when upwelled water that originates north of the bay flows across the bay mouth [6]. The generally lower FLH that prevailed by 3 May (Figure 4d) is consistent with the influence of strong wind stress causing enhanced turbulent vertical mixing of the upper water column and associated decreases in phytoplankton concentrations near the surface. The early onset of this upwelling event was closely monitored by AUV surveys (Figure 5).

The arrival of recently upwelled water is illustrated by the cooling of the upper water column by  $\sim 1.5^{\circ}\text{C}$  (Figure 5, left column). Corresponding with the arrival of cold recently upwelled water was a decrease in fluorometric chlorophyll concentrations and optical backscattering (Figure 5, middle two columns). Interpreted as a proxy for the concentration of particulate matter, optical backscattering data indicate a significant decrease in particle concentrations within the northern bay during the upwelling response. Using the ratio of optical backscattering to chlorophyll fluorescence (right column), we can distinguish particle types. The exceptionally high values of this ratio observed at the offshore end of the last

survey (Figure 5, lower right panel) were associated with suspended sediments that were transported with the upwelled water. An enhanced color HICO image from 27 April shows a whitish sediment plume originating from the coast north of the bay (not presented). Considering the potential transport of trace metals with sediments, this process has significant implications not only for phytoplankton productivity [27,28], but also for toxicity of toxigenic diatoms—as indicated by laboratory studies [29–31] and suggested from field studies [11,32].

**Figure 5.** Spring 2011 study: Autonomous underwater vehicle (AUV) data shows upwelling influence in the water column;  $b_b$  is optical backscattering. Rows a–c represent surveys in sequence (times shown in Figure 4a). The latitude/longitude/depth volume shown is the same in each data panel.

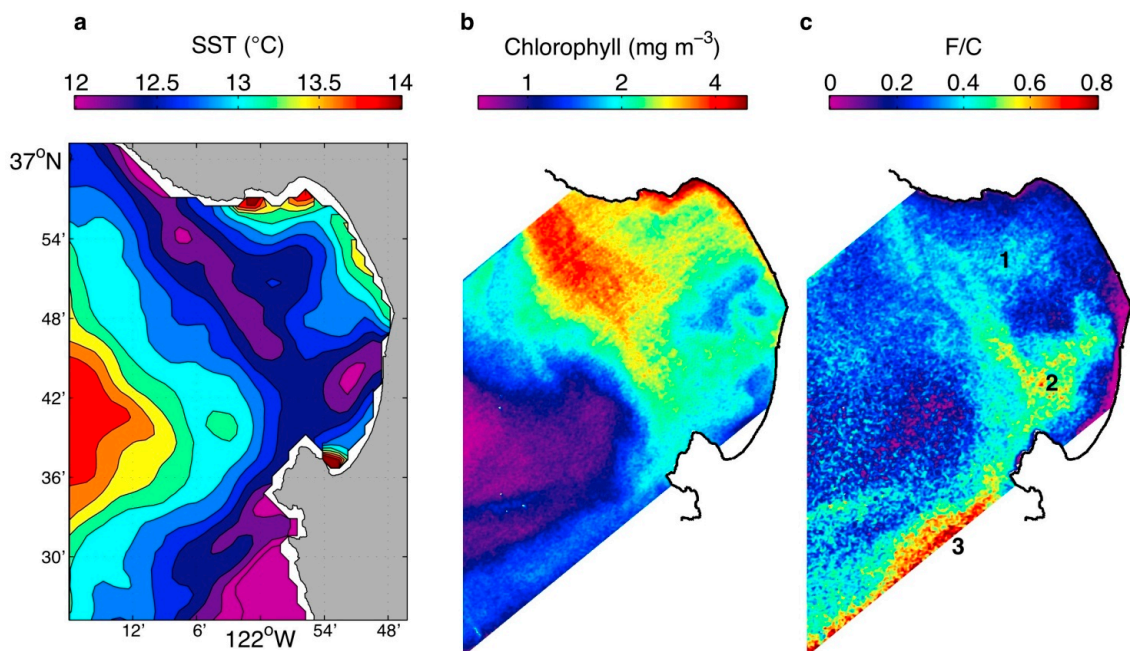


The first HICO image of the spring series, on 25 April, was acquired following a brief (~3 day) wind relaxation that followed weeks of strong and persistent upwelling (Figure 2). Warming and freshening of the upper water column occurred during the wind relaxation (Figure 2). This change in the physical environment is characteristic of wind relaxations [9,32] and consistent with the development of relatively quiescent conditions and a more stably stratified water column, with implications for response of the phytoplankton community to the preceding upwelling and associated nutrient supply. We examine physical and bio-optical patterns for this time to consider patchiness in phytoplankton bio-optical signal derived from HICO.

SST on 25 April showed a patchy remnant signature of the upwelling that preceded wind relaxation (Figure 3a). This relatively cool water extended across the mouth of Monterey Bay and within two lobes in the northern and southern bay. While evident in the color scaling of the SST time series (Figure 3), we more clearly illustrate this environmental structure in Figure 6a, for comparison with bio-optical characterizations.



**Figure 6.** Spring 2011 study: Relationships between thermal signatures of upwelling nutrient supply (a) and bio-optical characterization of phytoplankton (b,c). F/C is chlorophyll FLH (Figure 4b) divided by chlorophyll concentration (Figure 6b).



Chlorophyll FLH observed by HICO one hour after this SST image exhibited similar structure, with elevated FLH extending across the bay mouth and within two lobes extending into the northern and southern bay (Figure 4b). Chlorophyll concentration estimates from HICO also show this structure (Figure 6b). The FLH to chlorophyll ratio (F/C) revealed distinct patches (numbered in Figure 6c). F/C was much higher in the southern bay lobe (Figure 6c, #2) than in the northern bay lobe (Figure 6c, #1), corresponding with cooler water in the southern bay (Figure 6a). The relatively cool temperature in the southern bay suggests relatively greater nutrient input during the preceding upwelling period. Further, F/C was yet higher in a patch observed immediately outside of Monterey Bay (Figure 6c, #3). Nutrient supply to this area was evidently derived from both upwelling centers (Figure 6a), and upwelling filaments from both centers are known to merge in this region during strong upwelling (e.g., Figure 1). Thus, the combined physical and bio-optical patterns are consistent with different physiological responses of the phytoplankton along an environmental gradient of increasing nutrient supply, specifically greater quantum yield of fluorescence in regions of greater nutrient input [23,33]. It is also possible that the patchiness in F/C was due to similarly structured patchiness in phytoplankton communities [34], which in turn had different optical properties and physiology (absorption, scattering, quantum yield of fluorescence).

### 3.3. Fall 2011 Study

The fall study coincided with the warmest water conditions of the year (Figure 2). A clear HICO image acquired on 26 October (time shown in Figure 2) supported examination of phytoplankton ecotypes (Figure 7).

Chlorophyll and FLH exhibited similar patterns, however distinct patches were evident. One patch was in the northern bay, where a narrow filament extending from the coastal boundary exhibited elevated FLH (arrow in Figure 7b), compared to chlorophyll (Figure 7a). Applying the MCI algorithm to the HICO data further revealed distinction of this patch, which exhibited elevated reflectance in the near-infrared. This signal indicates dense accumulations of phytoplankton near the surface [24]. Such dense “red tide” patches are most commonly observed during the warm, stratified fall season in this region of the bay [9,32,35–37], and they have been linked to HAB effects [12]. Although at coarser spatial resolution, the MERIS satellite sensor also detected this distinct bloom patch in northern Monterey Bay on 26 October (Figure 8a). Further, a time-series from MERIS revealed that this bloom increased in intensity and spatial scale during the following week (Figure 8a–d). MERIS coverage of the entire bay confirmed that throughout its expansion this distinct bloom remained within the domain shown in Figure 8. *In situ* optical measurements for ground-truth of the remote sensing data were acquired on 28 October (Figure 9), at the location shown in Figure 8b (white +), less than one hour after the MERIS image was acquired.

Patchiness at a scale finer than that resolved by the MERIS image may have influenced the *in situ* optical measurements. However, the location of *in situ* sensing relative to the bloom distribution evident in the MERIS image indicates that the *in situ* measurements were made in an area where MCI values were comparable to the maximum observed on 26 October (cf. Figures 8a,b). Thus, we compare the *in situ* data from 28 October to the HICO spectra from 26 October for the red tide patch (Figure 7), assuming that each represents signal of enhanced reflectance in the near-infrared from the same bloom type. This comparison (Figure 9) shows similar spectral shapes at wavelengths greater than  $\sim 570$  nm, and divergence of spectral shapes at shorter wavelengths for different atmospheric correction methods. The similar spectral shape in both *in situ* and atmospherically corrected HICO data across the reflectance peak centered near 700 nm, *i.e.*, the optical signal of the bloom, supports application of this spectral shape algorithm to describing the bloom.

**Figure 7.** Fall 2011 study: Distinguishing a “red tide” bloom patch with HICO spectral and spatial resolution; MCI is Maximum Chlorophyll Index (Section 2.2). The HICO image was collected on 26 October 2011 at 15:33 local time. The white circle in the MCI map (panel c, zoom) defines the center location for which  $3 \times 3$  pixel mean spectra are presented (Figure 9).

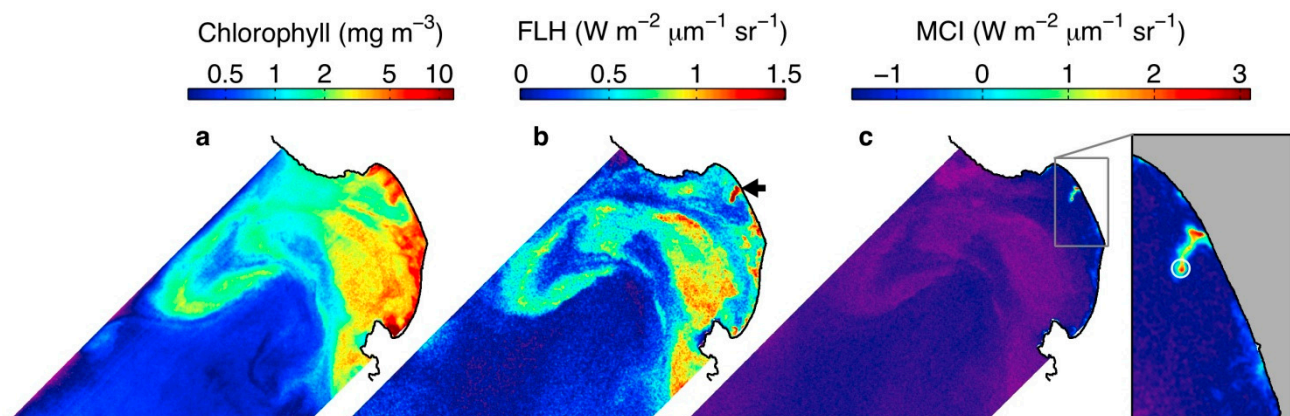


**Figure 8.** Fall 2011 study: Expansion of the red tide bloom, as described by MERIS MCI. The 26 October image was acquired at 11:28 local time, 4 hours and 5 minutes before the HICO image (Figure 7c). Note the different MCI color scales in comparing Figures 7c and 8a.

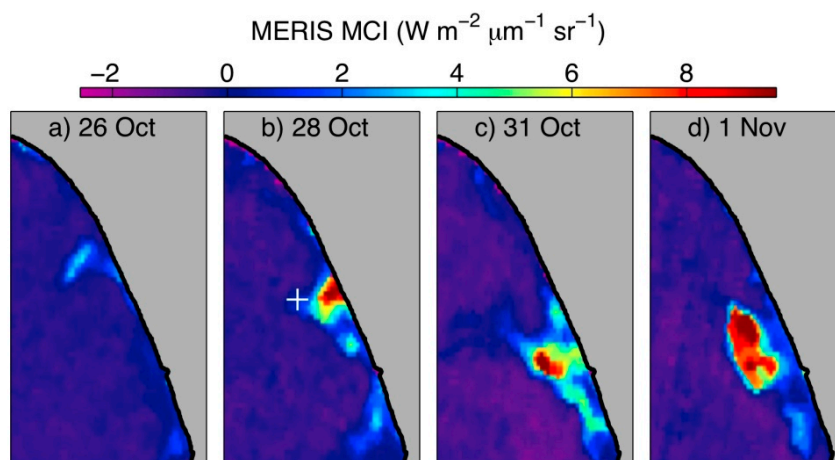
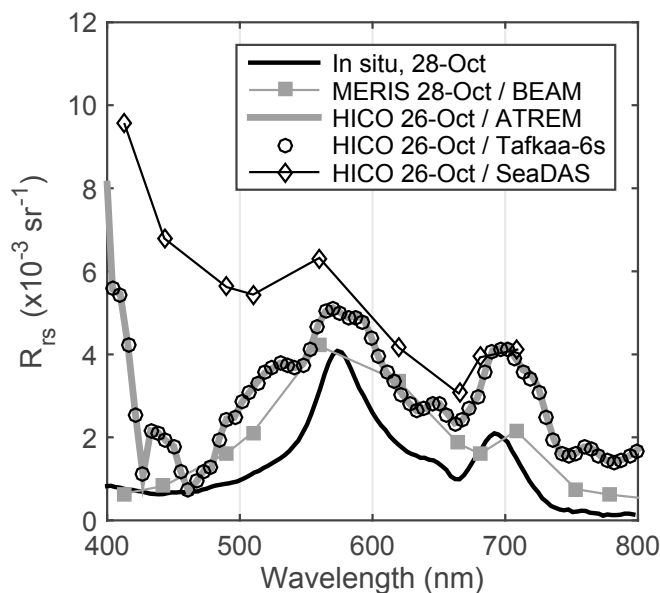


**Figure 9.** Fall 2011 study: Ground truth optical measurements acquired along the periphery of a red tide patch on 28 October 2011 (location shown in Figure 8b). The *in-situ*  $R_{rs}$  spectrum was acquired 59 min after the MERIS image. HICO spectra are  $3 \times 3$  pixel means from the location shown in Figure 7c (zoom panel). The Tafkaa 6s and ATREM results are nearly identical, and the lines are completely overlaid at the resolution of this figure.



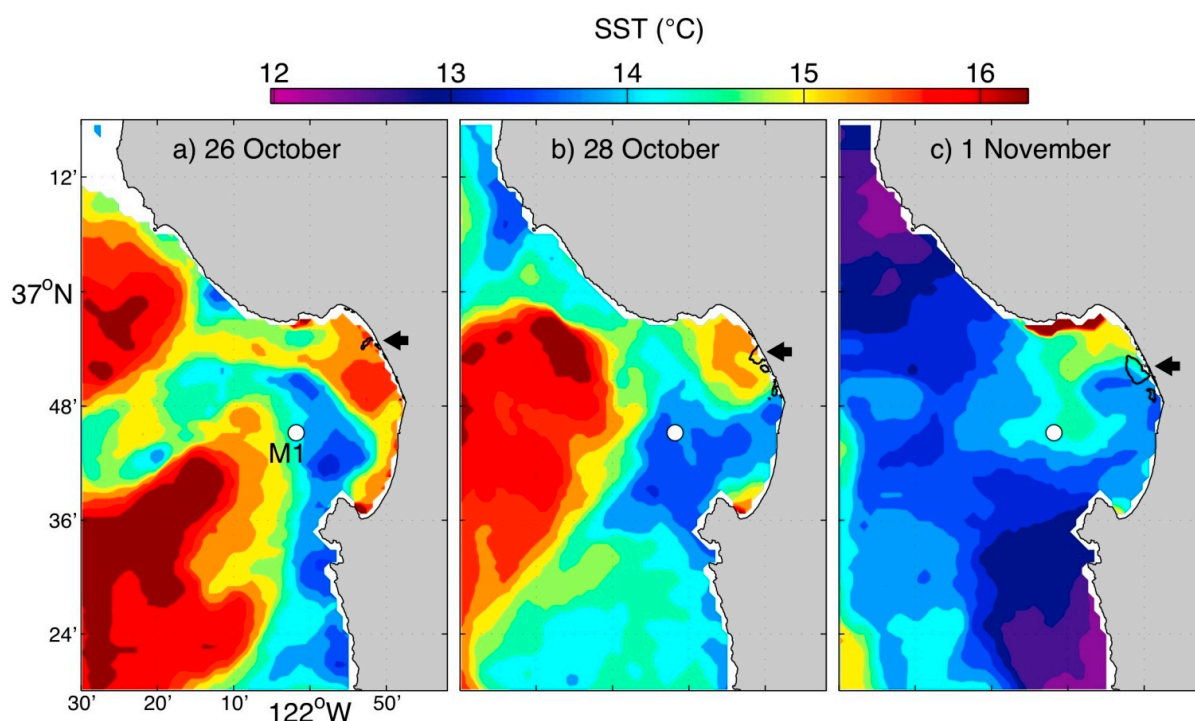
To investigate the processes underlying expansion of this distinct bloom type (Figure 8), we examine regional SST patterns during the same period (Figure 10). In each image, the domain of the bloom patch is overlaid (as indicated by the arrows in Figure 10).

Activity of the upwelling centers north and south of the bay increased during this period, and cooling occurred throughout the region. This was associated with the return of upwelling favorable winds following a minimum in wind speed on 26 October (Figure 2). On 26 October, the small bloom patch was located within relatively warm waters of the northeastern bay, and a cool plume extended



from the coast south of Monterey Bay, northward across the mouth of the bay (Figure 10a). This filament was detected at mooring M1 the previous day (sudden cooling before the image acquisition time indicated in Figure 2). In addition to local cooling of 3 °C, nitrate concentrations at the surface increased by  $\sim 5\mu\text{M}$  (data viewable at <http://www.mbari.org/lobo/loboviz.htm>), confirming the potential of this water to enrich nutrient supply to phytoplankton. As upwelling increased, the nutrient-enriched cold filament was transported into the nearshore environment of the bloom patch (Figure 10b). By 1 November, the expanding bloom was observed within a more distinct frontal zone between the warm resident bay waters and the intruding cool waters (Figure 10c). The intrusion was apparently linked to a cyclonic flow within the bay, as indicated by the adjacent cool/warm anomalies (Figure 10b, c).

**Figure 10.** Fall 2011 study: Processes of bloom growth. Black contours overlaid on the SST images (indicated by arrows) correspond with the red tide bloom patches shown in Figure 8.

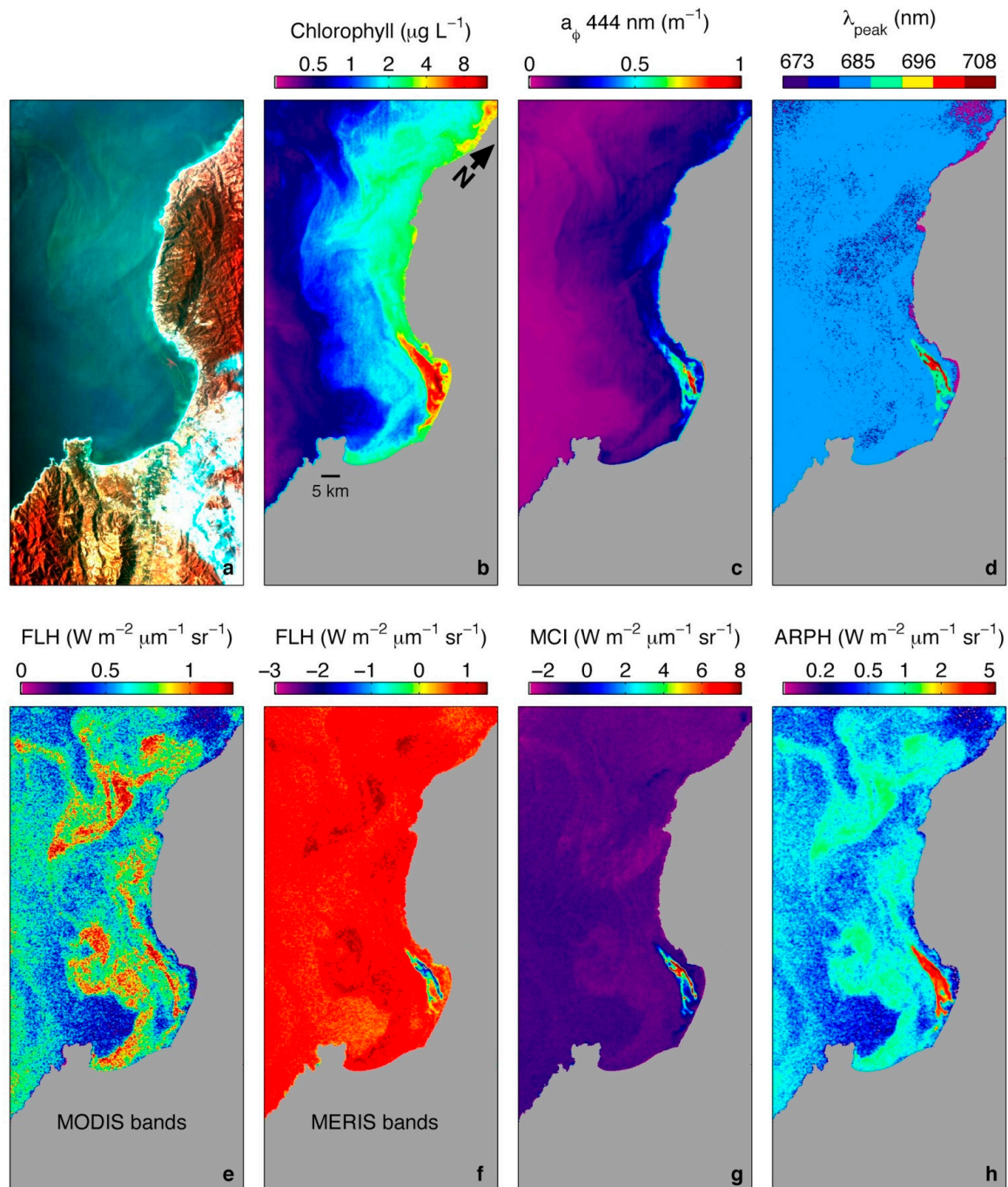


### 3.4. Examination of Algorithms for Characterization of Phytoplankton

Examination of algorithms for characterization of phytoplankton from HICO data is best supported by images that contain signals from a range of ecotypes. The fall 2011 study included a small “red tide” bloom that was optically distinguishable (previous section). However, an image from 6 November 2012 contained much greater signal range, and we use this image to examine the strengths and limitations of different algorithms (Figure 11). The pseudo true-color HICO image indicates great patchiness and suggests different phytoplankton ecotypes across the range of blue, green and brown water color (Figure 11a). Although a light atmospheric haze is evident in the image, a swath of brown across the northern bay stands out. Results of both band-ratio chlorophyll and IOP algorithms distinguish this brown water, which contained the highest values of both parameters (Figure 11b,c;  $a_{\phi 444}$  is phytoplankton absorption at 444 nm). This dense bloom is further distinguished by identification of the wavelength at which the reflectance spectrum peaked in the red to near-infrared

range (Figure 11d). Extending well beyond the chlorophyll fluorescence peak wavelength ( $\sim 683$  nm), this patch exhibited spectral peaks at wavelengths up to 708 nm, characteristic of intense “red tide” blooms [24] previously observed in this region with satellite and airborne remote sensing [36,37].

**Figure 11.** Phytoplankton characterization from a suite of algorithms. The HICO image was acquired on 6 November 2012. The enhanced color image (a) used bands centered at the 466 nm (blue), 554 nm (green), and 708 nm (near infrared, to emphasize signal of the red tide).

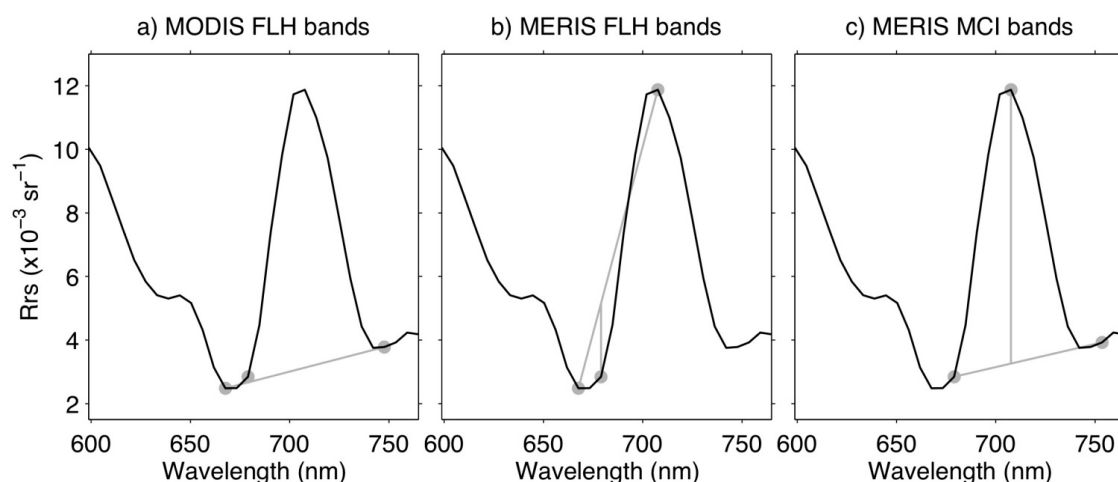


Next we examine a series of results from the linear baseline algorithms (LBAs), also known as spectral shape algorithms [38]. No distinction of the intense bloom patch (Figure 11a–d) is evident in

FLH computed using MODIS FLH bands (Figure 11e). Similar FLH levels are indicated in the intense bloom as in a large phytoplankton patch north of the bay, which exhibited much lower chlorophyll and  $a_{\phi 444}$  (Figure 11b,c). The reason for this lack of distinction is illustrated in Figure 12a. The shift of the reflectance peak into the near-infrared, caused by the extremely high concentration of phytoplankton near the surface, placed the bloom signal to the long wavelength side of center wavelength used by the MODIS FLH algorithm. The spectral peak shift was more moderate in the bloom patch observed on 26 October 2011 (Figure 9), thus placing the peak closer to the FLH algorithm center wavelength and yielding greater distinction of the patch in FLH (Figure 7b).

The intense bloom patch of 6 November 2012 was distinguished in FLH computed using MERIS bands (Figure 11f), however the algorithm quantifies it as the largest negative anomaly within the image. The reason for this inversion of bloom optical signal is illustrated in Figure 12b. The shift of the reflectance peak into the near-infrared lifts the long-wavelength end of the baseline, thus placing reflectance at the center wavelength of the MERIS FLH algorithm below the baseline. Such negative spectral shape has been used to detect cyanobacterial blooms in the Laurentian Great Lakes with both MERIS and MODIS data [38,39]. The intense bloom patch is effectively isolated by the MCI algorithm (Figure 11g), which was specifically designed to quantify strong near-infrared reflectance from this bloom type (Figure 12c). However, one consequence of isolating this spectral feature with this method is computation of the lowest MCI values in waters that have moderately high FLH (Figure 11e–g). This is because the MCI center wavelength falls in a trough of a spectrum characterized by ordinary chlorophyll fluorescence. Spatial patterns of intense bloom signal in MCI (Figure 11g) chlorophyll (Figure 11b) and  $a_{\phi 444}$  (Figure 11c) are distinct, suggesting considerable patchiness of phytoplankton community composition and/or physiological state within the bloom patch.

**Figure 12.** Linear baseline algorithm (LBA) performance relative to the intense bloom spectrum from the 6 November 2012 HICO image (Figure 11). The spectrum is an average computed from pixels exhibiting a peak in the HICO 708 nm band. Band centers (gray circles) for each algorithm are the HICO band center wavelengths listed in Table 1.



Each LBA was designed for a specific purpose using data from multispectral sensing. None was designed for hyperspectral sensing, and none consistently characterize spatial patterns of phytoplankton optical signal across the full range of phytoplankton ecotypes and bloom intensities.

Accurate description of variation in the spectral shape and intensity of phytoplankton reflectance requires algorithms that adapt their function according to the attributes of the reflectance spectrum itself. The maximum peak-height (MPH) is one such algorithm designed for MERIS multispectral data [40]. It was developed for operational determination of trophic status and indication of potentially harmful phytoplankton blooms in coastal and inland systems. MPH uses a baseline subtraction procedure, as in the FLH algorithm. While the short wavelength end of the baseline for MPH is the same as that used for MERIS FLH (665 nm), the long wavelength end is greater than that used for FLH (885 nm *versus* 709 nm). This is to enable quantification of signal caused by exceptionally dense cyanobacterial blooms. MPH computes the height of the dominant peak within the wavelength range of the baseline, at band-center wavelengths of 681, 709 or 753 nm, as caused by the balance of sun-induced chlorophyll fluorescence and particulate backscatter.

To more effectively localize the reflectance peak caused by phytoplankton in the 6 November 2012 HICO image, and to more consistently quantify phytoplankton optical signal across the different population types, we apply adaptation to the attributes of the reflectance spectrum itself in an algorithm termed adaptive reflectance peak height (ARPH). We do not require the wide baseline of MPH and thus set baseline wavelengths to the HICO center wavelengths nearest those used for MODIS FLH (Table 1), which take into consideration the influence of oxygen and water vapor absorption on spectral shape [23], and which are well-placed for characterization of optical signal from phytoplankton populations in Monterey Bay. We also constrain more narrowly the wavelength range for adaptive peak localization and quantification. The upper wavelength is constrained to <710 nm to exclude kelp forest reflectance evident in the image while including the maximum wavelength of peak reflectance in the phytoplankton red tide bloom (Figure 11d). The lower wavelength is constrained based on the observed minimum wavelength at which the red tide bloom exhibited distinction in its spectral peak, 690 nm (Figure 11d). With these constraints ARPH allowed adaptive quantification of phytoplankton optical signal across four HICO bands centered at 690, 696, 702 and 708 nm. Outside this range ARPH is equivalent to the MODIS FLH algorithm using HICO's nearest spectral bands (Table 1). Results from the ARPH algorithm illustrate effective adaptation using the spectral resolution of HICO (Figure 11h). ARPH provides a more consistent characterization of phytoplankton optical signal than any of the other algorithms. Like MODIS FLH, ARPH represents ordinary chlorophyll fluorescence consistently (Figure 11e,h). However, unlike MODIS FLH, ARPH distinguishes the extreme bloom patch that is evident in chlorophyll,  $a_{\phi 444}$  and reflectance peak wavelength (Figure 11b–d). Further, ARPH avoids the confused mixture of negative and positive anomalies caused by displacement of the reflectance peak within the red to near-infrared range, as described for MERIS FLH and MCI (Figure 11 f,g; Figure 12). The principle of MPH, as applied to HICO data in ARPH, is promising.

The spatial and spectral resolution of HICO and the growing archive of HICO image data in diverse aquatic environments will augment the development of methods to effectively characterize phytoplankton by remote sensing. Satellite remote sensing of freshwater cyanobacterial blooms has effectively used data of relatively coarse spatial and spectral resolution [38–40]; HICO's greater spatial and spectral resolutions enable more effective study of the patchiness and ecology of such blooms. Beyond the spectral analysis methods explored here are a host of algorithms designed for laboratory spectral analysis that can now be applied to HICO images [41]. An artificial neural network approach that analyzes ecological and geographical knowledge together with remotely sensed bio-optical and

physical parameters has been applied to predict phytoplankton functional types (PFTs) in the North Atlantic [42], and hyperspectral remote sensing data may enhance the effectiveness of this approach. Distinction of coccolithophore blooms has employed hyperspectral remote sensing data and differential optical absorption spectroscopy analysis [43]. Discrimination of phytoplankton pigment assemblages in the open ocean during non-bloom conditions had employed cluster analysis of *in situ* optical data, including measurements of multispectral remote sensing reflectance and hyperspectral absorption [44]. HICO offers the opportunity to extend these analysis methods to high-resolution remotely sensed data.

#### 4. Conclusions

Coastal ocean environments are profoundly important to global ecology, and they are major societal drivers through their support of living and mineral resource extraction, recreation, and tourism. Effective management of these vital environments requires comprehensive multidisciplinary understanding. Remote sensing provides one of the most effective tools for understanding coastal ecosystems and their connections to the greater ocean and land interfaces. As with any research endeavor, the closer we look, the more we learn. With its enhanced spatial and spectral resolution, HICO provides just such an opportunity to look more closely at the highly complex processes that drive coastal ecology. The examples presented in this study represent a small fraction of the HICO images of Monterey Bay, and a yet smaller fraction of the 8600 HICO images acquired worldwide. Studies such as this provide the opportunity to explore utilization of enhanced remote sensing resolutions, toward advancing ecological knowledge, environmental management, and design of future sensors. In particular the future NASA ocean color sensors PACE, GEO-CAPE and HypSPIRI are all proposed as hyperspectral imagers. HICO data provides an opportunity to develop new hyperspectral algorithms and evaluate spectral and spatial sampling and signal-to-noise requirements for these sensors.

#### Acknowledgments

JPR was supported by MBARI, through a grant from the David and Lucile Packard Foundation. RMK was supported by NASA Award # NNX09AT01G-01-D. HICO was operated under ONR sponsorship by NRL during the period of this study. We thank J. Nahorniak for managing the OSU portal for HICO data acquisition requests and data access. AVHRR SST and MERIS L2 MCI images were provided by D. Foley of NOAA CoastWatch. Updated equations for the QAA algorithm were provided by Z. Lee. Comments by anonymous reviewers supported significant improvement of the original draft of this manuscript. This is a contribution to the GEOHAB Core Research Project on HABs in Upwelling Systems.

#### Author Contributions

All co-authors contributed to the scientific content and authorship of this manuscript. COD led HICO data acquisition and atmospheric correction efforts, which were conducted by NBT and BCG. RMK provided *in situ* optical measurements to ground truth atmospherically corrected remote sensing

data. JPR led the study, analysis of remote sensing and *in situ* data, and manuscript preparation with all co-authors.

## Conflicts of Interest

The authors declare no conflict of interest.

## References

1. Lucke, R.L.; Corson, M.; McGlothlin, N.R.; Butcher, S.D.; Wood, D.L.; Korwan, D.R.; Li, R.R.; Snyder, W.A.; Davis, C.O.; Chen, D.T. Hyperspectral imager for the coastal ocean: Instrument description and first images. *Appl. Opt.* **2011**, *50*, 1501–1516.
2. Corson, M.R.; Davis, C.O. A new view of coastal oceans from the space station. *Eos Trans. Am. Geophys. Union* **2011**, *92*, 161–162.
3. Davis, C.O.; Bowles, J.; Leathers, R.A.; Korwan, D.; Downes, T.V.; Snyder, W.A.; Rhea, W.J.; Chen, W.; Fisher, J.; Bissett, W.P.; *et al.* Ocean PHILLS hyperspectral imager: Design, characterization, and calibration. *Opt. Express* **2002**, *10*, 210–221.
4. Barber, R.T.; Smith, R.L. Coastal Upwelling Ecosystems. In *Analysis of Marine Ecosystems*; Longhurst, A.R., Ed.; Academic Press: New York, NY, USA, 1981; pp. 31–68.
5. Breaker, L.C.; Broenkow, W.W. The circulation of Monterey Bay and related processes. *Oceanogr. Mar. Biol. Annu. Rev.* **1994**, *32*, 1–64.
6. Rosenfeld, L.K.; Schwing, F.B.; Garfield, N.; Tracy, D.E. Bifurcated flow from an upwelling center: A cold water source for Monterey Bay. *Cont. Shelf Res.* **1994**, *14*, 931–964.
7. Woodson, C.B.; Eerkes-Medrano, D.I.; Flores-Morales, A.; Foley, M.M.; Henkel, S.K.; Hessian-Lewis, M.; Jacinto, D.; Needles, L.; Nishizaki, M.T.; O’Leary, J.; *et al.* Local diurnal upwelling driven by sea breezes in northern Monterey Bay. *Cont. Shelf Res.* **2007**, *27*, 2289–2302.
8. Shea, R.E.; Broenkow, W.W. The role of internal tides in the nutrient enrichment of Monterey Bay, California. *Estuar. Coast. Shelf Sci.* **1982**, *15*, 57–66.
9. Ryan, J.P.; McManus, M.A.; Sullivan, J.M. Interacting physical, chemical and biological forcing of phytoplankton thin-layer variability in Monterey Bay, California. *Cont. Shelf Res.* **2010**, *30*, 7–16.
10. Kudela, R.; Pitcher, G.; Probyn, T.; Figueiras, F.; Moita, T.; Trainer, V. Harmful algal blooms in coastal upwelling systems. *Oceanography* **2005**, *18*, 184–197.
11. Ryan, J.; Greenfield, D.; Marin III, R.; Preston, C.; Roman, B.; Jensen, S.; Pargett, D.; Birch, J.; Mikulski, C.; Doucette, G.; *et al.* Harmful phytoplankton ecology studies using an autonomous molecular analytical and ocean observing network. *Limnol. Oceanogr.* **2011**, *56*, 1255–1272.
12. Jessup, D.A.; Miller, M.A.; Ryan, J.P.; Nevins, H.M.; Kerker, H.A.; Mekebri, A.; Crane, D.B.; Johnson, T.A.; Kudela, R.M. Mass stranding of marine birds caused by a surfactant-producing red tide. *PLoS ONE* **2009**, doi:10.1371/journal.pone.0004550.
13. Kudela, R.M.; Lane, J.; Cochlan, W. The potential role of anthropogenically derived nitrogen in the growth of harmful algae in California, USA. *Harmful Algae* **2008**, *8*, 103–110.
14. Kudela, R.M., University of California, Santa Cruz, CA, USA; Ryan, J.P. Monterey Bay Aquarium Research Institute, Moss Landing, CA, USA. Unpublished data, 2007–2009.
15. HICO. Available online: <http://hico.coas.oregonstate.edu>. (accessed on 1 November 2013).



16. Gao, B.-C.; Davis, C.O. Development of a line-by-line-based atmosphere removal algorithm for airborne and spaceborne imaging spectrometers. *Proc. SPIE* **1997**, doi:10.1117/12.283822.
17. Montes, M.J.; Gao, B.-C.; Davis, C.O. *NRL Atmospheric Correction Algorithms for Oceans: Tafkaa User's Guide*; NRL Report NRL/MR/7230-04-8760; NRL: Washington, DC, USA, 2004. Available online: <http://www.dtic.mil/cgi-bin/GetTRDoc?AD=ADA422068> (accessed on 17 July 2015).
18. Bowles, J. The US Naval Research Laboratory, Washington, DC, USA. Private Communication, 2013.
19. O'Reilly, J.E.; Maritorena, S.; Siegel, D.; O'Brien, M.C.; Toole, D.; Mitchell, B.G.; Kahru, M.; Chavez, F.P.; Strutton, P.; Cota, G.; *et al.* Ocean Color Chlorophyll A Algorithms for SeaWiFS, OC2, and OC4: Version 4. In *SeaWiFS Postlaunch Calibration and Validation Analyses, Part 3*; Hooker, S.B., Firestone, E.R., Eds.; NASA Goddard Space Flight Center: Greenbelt, MD, USA, 2000; Volume 11, pp. 9–23.
20. Lee, Z.P.; Carder, K.L.; Arnone, R.A. Deriving inherent optical properties from water color: A multiband quasi-analytical algorithm for optically deep waters. *Appl. Opt.* **2002**, *41*, 5755–5756.
21. Lee, Z.P.; Carder, K.L. Absorption spectrum of phytoplankton pigments derived from hyperspectral remote-sensing reflectance. *Remote Sens. Environ.* **2004**, *89*, 361–368.
22. IOCCG. Available online: <http://www.ioccg.org/groups/software.html>. (accessed on 1 November 2013).
23. Letelier, R.M.; Abbott, M.R.; An analysis of chlorophyll fluorescence algorithms for Moderate Resolution Imaging Spectrometer (MODIS). *Remote Sens. Environ.* **1996**, *58*, 215–223.
24. Gower J.; King, S.; Borstad, G.; Brown, L. Detection of intense plankton blooms using the 709 nm band of the MERIS imaging spectrometer, *Int. J. Remote Sens.* **2005**, *26*, 2005–2012.
25. Ryan, J.P.; Fischer, A.M.; Kudela, R.M.; McManus, M.A.; Myers, J.S.; Paduan, J.D.; Ruhsam, C.M.; Woodson, C.B.; Zhang, Y. Recurrent frontal slicks of a coastal ocean upwelling shadow. *J. Geophys. Res.* **2010**, doi:10.1029/2010JC006398.
26. Bellingham, J.G.; Streitlien, K.; Overland, J.; Rajan, S.; Stein, P.; Stannard, J.; Kirkwood, W.; Yoerger, D. An Arctic basin observational capability using AUVs. *Oceanography* **2000**, *13*, 64–71.
27. Johnson, K.S.; Chavez, F.P.; Friederich, G.E. Continental-shelf sediment as a primary source of iron for coastal phytoplankton. *Nature* **1999**, *398*, 697–700.
28. Bruland, K.W.; Rue, E.L.; Smith, G.J. The influence of iron and macronutrients in coastal upwelling regimes off central California: Implications for extensive blooms of large diatoms. *Limnol. Oceanogr.* **2001**, *46*, 1661–1674.
29. Rue, E.L.; Bruland, K.W. Domoic acid binds iron and copper: A possible role for the toxin produced by the marine diatom *Pseudo-nitzschia*. *Mar. Chem.* **2001**, *76*, 127–134.
30. Maldonado M.T.; Hughes, M.P.; Rue, E.L.; Wells, M.L. The effect of Fe and Cu on growth and domoic acid production by *Pseudo-nitzschia multiseries* and *Pseudo-nitzschia australis*. *Limnol. Oceanogr.* **2002**, *47*, 515–526.
31. Rhodes, L.; Selwood, A.; McNabb, P.; Briggs, L.; Adamson, J., van Ginkel, R.; Laczka, O. Trace metal effects on the production of biotoxins by microalgae. *Afr. J. Mar. Sci.* **2006**, *28*, 393–397.
32. Ryan, J.P.; McManus, M.A.; Kudela, R.M.; Lara Artigas, M.; Bellingham, J.G.; Chavez, F.P.; Doucette, G.; Foley, D.; Godin, M.; Harvey, J.B.J.; *et al.* Boundary influences on HAB phytoplankton ecology in a stratification-enhanced upwelling shadow. *Deep Sea Res. Part II Top. Stud. Oceanogr.* **2013**, in press.



33. Huot, Y.; Franz, B.A.; Fradette, M. Estimating variability in the quantum yield of Sun-induced chlorophyll fluorescence: A global analysis of oceanic waters. *Remote Sens. Environ.* **2013**, *132*, 238–253.
34. Abbott, M.R.; Brink, K.H.; Booth, C.R.; Blasco, D.; Swenson, M.S.; Davis, C.O.; Codispoti, L.A. Scales of variability of bio-optical properties as observed from near-surface drifters. *J. Geophys. Res. Ocean* **1995**, *100*, 13345–13367.
35. Kudela, R.M.; Ryan, J.P.; Blakely, M.D.; Lane, J.Q.; Peterson, T.D. Linking the physiology and ecology of *Cochlodinium* to better understand harmful algal bloom events: A comparative approach. *Harmful Algae* **2008**, *7*, 278–292.
36. Ryan, J.P.; Gower, J.F.R.; King, S.A.; Bissett, W.P.; Fischer, A.M.; Kudela, R.M.; Kolber, Z.; Mazzillo, F.; Rienecker, E.V.; Chavez, F.P. A coastal ocean extreme bloom incubator. *Geophys. Res. Lett.* **2008**, doi:10.1029/2008GL034081.
37. Ryan, J.P.; Fischer, A.M.; Kudela, R.M.; Gower, J.F.R.; King, S.A.; Marin, R., III; Chavez, F.P. Influences of upwelling and downwelling winds on red tide bloom dynamics in Monterey Bay, California. *Cont. Shelf Res.* **2009**, *29*, 785–795.
38. Wynne, T.T.; Stumpf, R.P.; Tomlinson, M.C.; Warner, R.A.; Tester, P.A.; Dybie, J.; Fahnenstiel, G.L. Relating spectral shape to cyanobacterial blooms in the Laurentian Great Lakes. *Int. J. Remote Sens.* **2008**, *29*, 3665–3672.
39. Wynne, T.T.; Stumpf, R.P.; Briggs, T.O. Comparing MODIS and MERIS spectral shapes for cyanobacterial bloom detection. *Int. J. Remote Sens.* **2013**, *34*, 6668–6678.
40. Matthews, M.W.; Bernard, S.; Robertson, L. An algorithm for detecting trophic status (chlorophyll-a), cyanobacterial-dominance, surface scums and floating vegetation in inland and coastal waters. *Remote Sens. Environ.* **2012**, *124*, 637–652.
41. Tufillaro, N. The Shape of Ocean Color. In *Topology and Dynamics of Chaos*; Letellier, C., Gilmore, R. Eds.; World Scientific Publishing: Singapore, 2013; pp. 251–268.
42. Raitos, D.E.; Lavender, S.J.; Maravelias, C.D.; Haralabous, J.A.; Richardson, J.; Reid, P.C. Identifying four phytoplankton functional types from space: An ecological approach. *Limnol. Oceanogr.* **2008**, *53*, 605–613.
43. Sadeghi, A.; Dinter, T.; Vountas, M.; Taylor, B.; Altenburg-Soppa, M.; Bracher, A. Remote sensing of coccolithophore blooms in selected oceanic regions using the PhytoDOAS method applied to hyper-spectral satellite data. *Biogeosciences* **2012**, *9*, 2127–2143.
44. Torrecilla, E.; Stramski, D.; Reynolds, R.A.; Millán-Núñez, E.; Piera, J. Cluster analysis of hyperspectral optical data for discriminating phytoplankton pigment assemblages in the open ocean. *Remote Sens. Environ.* **2011**, *115*, 2578–2593.